








RESEARCH ARTICLE

Numerical study of oil–water emulsion formation in stirred vessels: effect of impeller speed

Fuyue Liang¹ , Lyes Kahouadji^{1,*} , Juan Pablo Valdes¹ , Seungwon Shin² , Jalel Chergui³ , Damir Juric^{3,4}  and Omar K Matar¹ 

¹Department of Chemical Engineering, Imperial College London, South Kensington Campus, London SW7 2AZ, UK

²Department of Mechanical and System Design Engineering, Hongik University, Seoul 04066, Republic of Korea

³Université Paris Saclay, Centre National de la Recherche Scientifique (CNRS), Laboratoire Interdisciplinaire des Sciences du Numérique (LISN), 91400 Orsay, France

⁴Department of Applied Mathematics and Theoretical Physics, University of Cambridge, Centre for Mathematical Sciences, Wilberforce Road, Cambridge CB3 0WA, UK

*Corresponding author. E-mail: l.kahouadji@imperial.ac.uk

Received: 4 February 2022; **Revised:** 18 August 2022; **Accepted:** 29 September 2022

Keywords: Oil–water emulsion; Multiphase mixing; LES

Abstract

The mixing of immiscible oil and water by a pitched blade turbine in a cylindrical vessel is studied numerically. Three-dimensional simulations combined with a hybrid front-tracking/level-set method are employed to capture the complex flow and interfacial dynamics. A large eddy simulation approach, with a Lilly–Smagorinsky model, is employed to simulate the turbulent two-phase dynamics at large Reynolds numbers $Re = 1802$ – $18\,026$. The numerical predictions are validated against previous experimental work involving single-drop breakup in a stirred vessel. For small Re , the interface is deformed but does not reach the impeller hub, assuming instead the shape of a Newton’s Bucket. As the rotating speed increases, the deforming interface attaches to the impeller hub which leads to the formation of long ligaments that subsequently break up into small droplets. For the largest Re studied, the system dynamics becomes extremely complex wherein the creation of ligaments, their breakup and the coalescence of drops occur simultaneously. The simulation outcomes are presented in terms of spatio-temporal evolution of the interface shape and vortical structures. The results of a drop size analysis in terms of the evolution of the number of drops, and their size distribution, is also presented as a parametric function of Re .

Impact Statement

Emulsions are of primary interest in modern engineering research given their heavy usage both in our daily life (e.g. food and cosmetics) and in high-end industrial applications (e.g. drug development). An insufficient understanding of mixing dynamics has commonly led to over-design practices to guarantee a certain threshold of quality and performance, which can be easily overlooked, causing severe economic and environmental consequences. Attention has been focused previously on the effect of operational parameters (e.g. impeller speed) on mixing performance, which, however, has led to limited insight due to the difficulty in obtaining clear visualisation of the liquid–liquid mixing process. The results from this study are intended to provide a detailed picture of the underlying physics and interfacial dynamics within mixing systems as a function of impeller speed, attained through our high-fidelity three-dimensional numerical simulations. Based on this, substantial improvement to optimal operation at the design stage can be achieved.

1. Introduction

The applications of the mixing of two immiscible liquids by a stirrer range from the production of daily necessities (e.g. food and cosmetics) to large-scale industrial processing (e.g. petrochemicals and pharmaceuticals). Mixing in a stirred vessel is the most common operation unit in this field where a rotating impeller controls the continuous-phase flow dynamics and exerts an influence on the dispersed-phase behaviour. The flow dynamics within such a system has attracted research interest for decades since it determines the interfacial area and, consequently, the product quality in addition to the efficiency of heat and mass transfer between the two liquid phases. At sufficiently large impeller rotational speeds, turbulent eddies are introduced by the rotating impeller, which subsequently interact with the dispersed phase giving rise to dispersed-phase deformation, ligament production and, finally, drop breakup; the competition between drop breakup and coalescence determines the dispersed drop numbers, their size distribution and therefore the interfacial area. From an industrial standpoint, the inherent complexity of these processes hampers the understanding and control of the flow dynamics and interface behaviours within a mixing vessel which are important for product design and scale-up.

Numerous researchers have conducted studies on the characteristic drop size distribution during the emulsification process (with a focus on d_{max} , the maximum stable drop diameter, and d_{32} , the Saunter mean drop diameter, typically) and investigated the effect of various parameters (e.g. the physical properties of the two phases, operating conditions and the design of the vessel and impeller) on drop breakup in stirred vessels; this has led to several reviews of this field (see, for instance, the work of Afshar Ghotli, Raman, Ibrahim, and Baroutian (2013) and Hasan (2017) and references therein). There have been many experiments on drop size distribution in liquid–liquid dispersions exemplified by the work of Wang and Calabrese (1986), Lovick, Mouza, Paras, Lye and Angeli (2005), El-Hamouz, Cooke, Kowalski, and Sharratt (2009), Boxall, Koh, Sloan, Sum and Wu (2010), Becker, Puel, Chevalier, and Sheibat-Othman (2014), De Hert and Rodgers (2017) and Naeeni and Pakzad (2019b). On the other hand, Hinze (1955) carried out pioneering work in this field proposing two dimensionless groups, the Weber number, We , and the viscosity group, Vi , to account for the contributions of the external and the dispersed-phase viscous forces to the drop breakup. The analysis of the correlation for d_{32} and d_{max} started with Sprow (1967) in which it was verified through his experimental data that $d_{32} = Cd_{max}$, where C is a proportionality constant. Later, Zhou and Kresta (1998a) reported that C varies with operating conditions and fluid properties. Although Pacek, Man, and Nienow (1998) doubted the relationship between d_{32} and d_{max} , several investigators adopted the assumption and modified it by considering the effect of dispersed-phase viscosity and volume fraction (Calabrese, Chang, & Dang, 1986; Kraume, Gäbler, & Schulze, 2004). More recently, the combination of population balance models with computational fluid dynamics (CFD) (Ramkrishna, 2000) has become widely used to predict the drop size distribution in stirred vessels (Naeeni & Pakzad, 2019a; Qin et al., 2016; Roudsari, Turcotte, Dhib, & Ein-Mozaffari, 2012).

The above mentioned determination of drop size distribution, however, does not provide clear insights into the interfacial phenomena during the breakup of drops and their re-coalescence in complex flow fields. Previous studies have reported that a dispersed drop experiences various stages before reaching an equilibrium size, which include random deformation, stretching and elongation (Andersson & Andersson, 2006; Nachtigall, Zedel, & Kraume, 2016; Sanjuan-Galindo, Soto, Zenit, & Ascanio, 2015). Although numerous experiments have been carried out to study drop breakup in stirred vessels (Calabrese et al., 1986; Giapos, Pachatouridis, & Stamatoudis, 2005; Maaß, Metz, Rehm, & Kraume, 2010; Stamatoudis & Tavlarides, 1985; Wang & Calabrese, 1986; Zhou & Kresta, 1998b), a number of contradictory conclusions remain in the literature. For example, Sathyagal, Ramkrishna, and Nar-simhan (1996) have found that the breakup rate decreases considerably with increasing dispersed-phase viscosity and interfacial tension, with a stronger dependence on the latter, while Kraume et al. (2004) suggested that the viscosity exerts a larger influence on the drop breakup. These contradictions may be ascribed to differences in the experimental set-ups used to capture the breakup process.

The results of single-drop breakup experiments have also been reported in the literature. [Konno, Aoki, and Saito \(1983\)](#) carried out the first single-drop experiment in three stirred vessels of different diameters where the authors tracked the drop breakup trajectory and reported the path length along with the distribution of breakup positions. [Maaß, Gäbler, Zaccone, Paschedag and Kraume \(2007\)](#) used a more sophisticated breakup cell device in which the continuous-phase fluid flows through a fixed single blade in a rectangular channel to produce a comparable flow field to a stirred liquid–liquid system, and a single drop is injected to mimic the breakup phenomena; this cell facilitated the recording of the breakup details. Subsequent studies adopted this set-up and reported data on breakup event location ([Maaß, Wollny, Sperling, & Kraume, 2009](#)), rate ([Maaß & Kraume, 2012](#)), mechanisms ([Nachtigall et al., 2012](#)) and deformation dynamics ([Nachtigall et al., 2016](#)).

In terms of numerical predictions of flows in stirred vessels, work in this area must overcome the significant challenges associated with simulating interfacial deformation in a drop-laden turbulent flow driven by a rotating impeller. Nevertheless, various approaches have been used including the volume-of-fluid ([Hirt & Nichols, 1981](#)), phase field ([Anderson, McFadden, & Wheeler, 1998](#); [Chiu & Lin, 2011](#)), front tracking ([Tryggvason et al., 2001](#); [Unverdi & Tryggvason, 1992](#)), level-set methods ([Sethian & Smereka, 2003](#)) and, recently, a newly method consisting of a weakly compressible homogeneous shear turbulence ([Scapin et al., 2022](#)). On the other hand, a large number of modelling techniques for stirred vessels have been developed such as the black-box ([Harvey & Greaves, 1982](#)), the multiple reference frame ([Luo & Gosman, 1994](#)) and sliding mesh ([Bakker, LaRoche, Wang, & Calabrese, 1997](#)) methods. The lattice Boltzmann method (LBM) has also been used to simulate flows in stirred vessels ([Derksen, 2003, 2011, 2012](#); [Derksen & Van den Akker, 1999](#); [Eggels, 1996](#); [Gillissen & Van den Akker, 2012](#); [Shu & Yang, 2018](#); [Tyagi, Roy, Harvey, & Acharya, 2007](#)); these studies have yielded flow field information only, rather than the detailed interfacial dynamics. [Scarbolo and Soldati \(2013\)](#) and [Scarbolo, Bianco, and Soldati \(2015\)](#) used a phase field approach to study drops deforming in a fully developed turbulent channel flow with a focus on the effect of the turbulent field on the droplet interface. [Scarbolo, Bianco, and Soldati \(2016\)](#) built on this previous work to study turbulence modification by the dispersed phase; subsequently, [Roccon, De Paoli, Zonta, and Soldati \(2017\)](#) extended this study to show that an increase in viscosity or interfacial tension decreases the breakup rate. [Albernaz, Do-Quang, Hermanson, and Amberg \(2017\)](#) used a hybrid LBM to study the deformation of a single drop in stationary isotropic turbulence while [Komrakova \(2019\)](#) applied a diffuse interface free energy LBM to examine single-drop breakup in homogeneous isotropic turbulence. These high-resolution simulations confirmed the presence of previously reported breakup mechanisms and elucidated an additional, so-called ‘burst breakup’ mechanism.

As the foregoing review indicates, there remains a gap in our understanding of all the stages of the emulsification process, from the onset of drop breakup through to the attainment of a dynamic steady state. Bridging this gap requires a transparent connection between the interfacial deformation, the prevailing flow conditions (parameterised by the impeller rotational speed) and their associated vortical structures. Although previous studies have suggested that increasing the impeller speed produces smaller droplets ([El-Hamouz et al., 2009](#); [Naeeni & Pakzad, 2019a](#); [Zhou & Kresta, 1998a](#)), such a connection has not been established. Remarkable improvements have been made for the numerical computation of interfacial singularities ([Chiappini, Sbragaglia, Xue, & Falcucci, 2019](#); [Di Ilio, Krastev, & Falcucci, 2019](#); [Falcucci & Ubertini, 2010](#)), but there remains a requirement of enormous resolution to track accurately these mechanisms. In an effort to address this in the present study, we will deploy massively parallel, three-dimensional, large eddy simulations of oil and water emulsification in a cylindrical vessel stirred by a pitched blade turbine, where the incompressible Navier–Stokes equations are resolved and the direct forcing method is employed to implement the simulation of impeller rotation. In particular, our simulations are combined with a hybrid front-tracking and level-set interface-capturing algorithm. This approach will provide detailed, high-fidelity visualisations of the intricate interfacial dynamics coupled to the turbulent flow fields, and will elevate our fundamental understanding and, ultimately, our control of the emulsification process. Allied to this, an analysis of the drop size distribution as a function of the

impeller speed will also be carried out; this analysis demonstrates that the number of dispersed drops is maximised for an intermediate value of the impeller rotational speed.

The rest of this article is organised as follows: § 2 describes the configurations, governing equations and the computational methods employed. Section 3 provides a comprehensive discussion of the vortical structures and interfacial dynamics inside the stirred vessel as a function of the impeller speed ($f = 1\text{--}10$ Hz with corresponding $Re = 1802\text{--}18\,026$ and $We = 2.19\text{--}219$), followed by an analysis of the drop size distribution. Finally, conclusions are summarised and ideas for future work are outlined in § 4.

2. Simulation configuration and methods

The configuration considered in this work is shown in figure 1(a). It is composed of a cylindrical vessel of diameter $T = 8.5$ cm filled with water in the lower half and oil in the upper half (volume fraction of oil, $\alpha = 0.5$). The impeller employed is a pitched blade turbine (PBT), which consists of four blades of 2.5 cm length, 1 cm height and 0.2 cm thickness. The PBT is immersed in the water phase with a clearance of $C = 1$ cm from the bottom of vessel, and rotates with frequency f . The impeller diameter is $D = 4.25$ cm which corresponds to an impeller-to-vessel diameter ratio of $D/T = 0.5$. A snapshot from a typical simulation is displayed in figure 1(b), which provides an example of the level of complexity associated with the flows under consideration in the present work.

Under the assumptions of incompressible and immiscible viscous fluids, the mass and momentum conservation equations are solved in a Cartesian domain $\mathbf{x} = (x, y, z) \in [0, 8.6]^2 \times [0, 12.75]$ cm

$$\nabla \cdot \bar{\mathbf{u}} = 0, \quad (2.1)$$

$$\rho \left(\frac{\partial \bar{\mathbf{u}}}{\partial t} + \bar{\mathbf{u}} \cdot \nabla \bar{\mathbf{u}} \right) = -\nabla \bar{p} + \nabla \cdot [(\mu + \rho C_s^2 \Delta^2 |\bar{\mathbf{S}}|)(\nabla \bar{\mathbf{u}} + \nabla \bar{\mathbf{u}}^T)] + \rho \mathbf{g} + \mathbf{F} + \mathbf{F}_{fsi}, \quad (2.2)$$

where $\bar{\mathbf{u}}$ and \bar{p} are the ensemble-averaged fluid velocity and pressure, respectively, t denotes time and \mathbf{g} is the gravitational acceleration. In (2.2), we use a single-field formulation for the density ρ and viscosity μ expressed by

$$\rho(\mathbf{x}, t) = \rho_o + (\rho_w - \rho_o)\mathcal{H}(\mathbf{x}, t), \quad (2.3)$$

$$\mu(\mathbf{x}, t) = \mu_o + (\mu_w - \mu_o)\mathcal{H}(\mathbf{x}, t), \quad (2.4)$$

where the subscripts o and w designate the oil and water phases, respectively. The indicator function \mathcal{H} , is essentially a numerical Heaviside function, zero in the oil phase and unity in the water phase. Here, \mathcal{H} is resolved with a sharp but smooth transition across 3–4 grid cells, and is generated using a vector distance function $\varphi(\mathbf{x})$, positive for the water phase and negative for the oil phase, computed directly from the tracked interface (Shin, Chergui, & Juric, 2017; Shin & Juric, 2009a). The density and viscosity of the water and oil phases are 998 kg m^{-3} and $10^{-3} \text{ Pa} \cdot \text{s}$, and 824 kg m^{-3} and $5.4 \times 10^{-3} \text{ Pa} \cdot \text{s}$, respectively; the interfacial tension is $\sigma = 0.035 \text{ N m}^{-1}$. The oil phase corresponds to a type of silicone oil used in previous work (Constante-Amores, 2021; Constante-Amores et al., 2021b; Ibarra, 2017).

A range of impeller rotation frequencies, $f = 1\text{--}10$ Hz, is studied which corresponds to $Re = 1802\text{--}18\,026$ and $We = 2.19\text{--}219$ where the Reynolds and Weber numbers are respectively given by

$$Re = \frac{\rho_w f D^2}{\mu_w}, \quad We = \frac{\rho_w f^2 D^3}{\sigma}, \quad (2.5a,b)$$

which provide a measure of the relative significance of inertial to viscous and interfacial tension forces. Here, D and fD are the characteristic length and velocity scales, respectively. The large Reynolds numbers in the upper end of the Re range motivate the use of a large eddy simulation approach; here, we employ a Smagorinsky turbulence model (Smagorinsky, 1963) which is included in (2.2) wherein

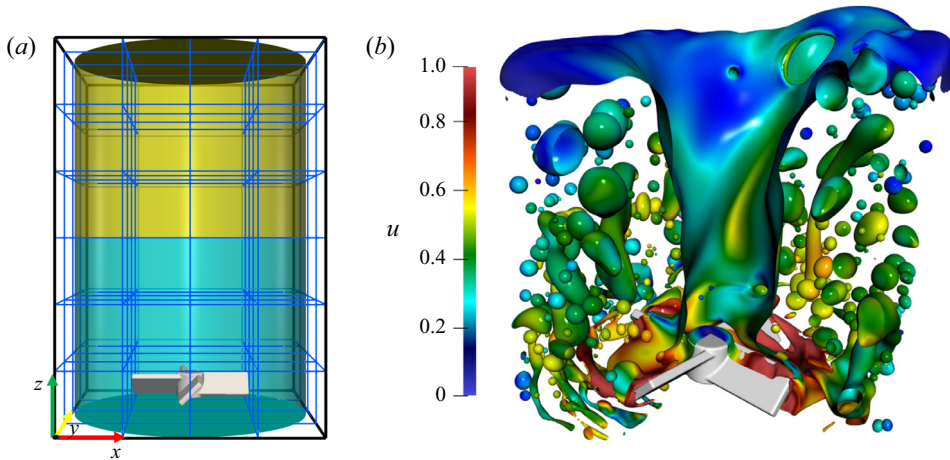


Figure 1. (a) Schematic illustration of the computational domain for the oil–water mixing system, which corresponds to a stirred vessel filled with oil and water in the upper and lower halves, respectively, with a pitched blade turbine immersed in the water phase. The domain is of size $8.6 \times 8.6 \times 12.75 \text{ cm}^3$ and it is divided into $4 \times 4 \times 6$ subdomains. The Cartesian structured grid per subdomain is 64^3 , which gives a total grid number of $256 \times 256 \times 384$. (b) An illustrative snapshot of the interface at $t = 25 \times T$ coloured by velocity field for $f = 7 \text{ Hz}$; here, a quarter of the interface is hidden to provide a clear view of the impeller and the interface in its vicinity.

C_s is the Smagorinsky–Lilly coefficient, $\Delta = V^{1/3}$ where V is the volume of a grid cell, $V = \Delta x \Delta y \Delta z$ and $|\bar{S}| = \sqrt{2\bar{S}_{ij}\bar{S}_{ij}}$ with \bar{S}_{ij} being the strain rate tensor:

$$\bar{S}_{ij} = \frac{1}{2} \left(\frac{\partial \bar{u}_i}{\partial x_j} + \frac{\partial \bar{u}_j}{\partial x_i} \right) \tag{2.6}$$

(Meyers & Sagaut, 2006; Pope, 2000, 2004). In the current work, $C_s = 0.2$, which is an intermediate value in the range 0.1–0.3 quoted in the literature (Deardorff, 1970; Lilly, 1966, 1967; McMillan & Ferziger, 1979; Pope, 2000); setting $C_s = 0$ eliminates the turbulence model and (2.2) reduces to the Navier–Stokes equations. Finally, we solve the large eddy simulation filtered equations without any specific turbulence model for the interface dynamics.

The forces \mathbf{F} and \mathbf{F}_{fsi} in (2.2) denote the local surface tension and the solid–fluid interaction forces, respectively, where \mathbf{F} is defined using a hybrid formulation (Shin et al., 2017, 2018)

$$\mathbf{F} = \sigma \kappa_H \nabla \mathcal{H}(\mathbf{x}, t), \tag{2.7}$$

in which σ , the surface tension, is assumed constant. In (2.7), κ_H is twice the mean interface curvature field calculated on an Eulerian grid using

$$\kappa_H = \frac{\mathbf{F}_L \cdot \mathbf{G}}{\sigma \mathbf{G} \cdot \mathbf{G}}, \tag{2.8}$$

in which \mathbf{F}_L and \mathbf{G} are given by

$$\mathbf{F}_L = \int_{\Gamma(t)} \sigma \kappa_f \mathbf{n}_f \delta_f(\mathbf{x} - \mathbf{x}_f) \, ds, \tag{2.9}$$

$$\mathbf{G} = \int_{\Gamma(t)} \delta_f(\mathbf{x} - \mathbf{x}_f) \, ds. \tag{2.10}$$

In these formulae, \mathbf{n}_f corresponds to the unit normal vector to the interface, and ds is the length of the interface element; κ_f is twice the mean interface curvature obtained from the Lagrangian interface. The geometric information corresponding to the unit normal \mathbf{n}_f and the length of the interface element ds in \mathbf{G} are computed directly from the Lagrangian interface and then distributed on an Eulerian grid using the discrete delta function and following an immersed boundary approach (Peskin, 1977). A detailed computation of the force and construction of the function field \mathbf{G} can be found in Shin (2007), Shin and Juric (2009a, 2009b) and Shin et al. (2017).

The Lagrangian interface is advected by integrating

$$\frac{d\mathbf{x}_f}{dt} = \mathbf{V}, \quad (2.11)$$

with a second-order Runge–Kutta method where the interface velocity \mathbf{V} is interpolated from the Eulerian velocity. Incorporating the complex geometry of the impeller and its rotation requires the implementation of the so-called direct forcing method (Mohd-Yusof, 1997; Fadlun, Verzicco, Orlandi, & Mohd-Yusof, 2000); this, in turn, is implemented by incorporating a fluid–solid interaction force \mathbf{F}_{fsi}^n into (2.2) defined numerically using the latest step of the temporal integration of (2.2)

$$\rho \frac{\bar{\mathbf{u}}^{n+1} - \bar{\mathbf{u}}^n}{\Delta t} = local^n + \mathbf{F}_{fsi}^n. \quad (2.12)$$

Here, ‘local’ represents the right-hand-side terms of (2.2) that comprise the convective, pressure gradient, viscous, turbulent, gravitational and surface tension force terms; the superscripts denote the discrete temporal step in the computation.

In the solid part of the domain corresponding to the impeller, the rotational motion \mathbf{V}^{n+1} is enforced

$$\bar{\mathbf{u}}^{n+1} = \mathbf{V}^{n+1} = 2\pi f((y - y_0), -(x - x_0)), \quad (2.13)$$

where $(x_0, y_0) = (4.25, 4.25)$ cm are the coordinates of the impeller axis. Hence, \mathbf{F}_{fsi}^n is given by

$$\mathbf{F}_{fsi}^n = \rho \frac{\mathbf{V}^{n+1} - \bar{\mathbf{u}}^n}{\Delta t} - local^n. \quad (2.14)$$

The no-slip condition is imposed on the velocity and the interface at the edge of the impeller parts.

The computational domain (see figure 1a) is a rectangular parallelepiped discretised by a uniform fixed three-dimensional finite-difference mesh and has a standard staggered marker-and-cell method cell arrangement (Harlow & Welch, 1965). The velocity components \bar{u} , \bar{v} and \bar{w} are defined on the corresponding cell faces while the scalar variables (pressure \bar{p} and the distance function ψ) are located at the cell centres. All spatial derivatives are approximated by second-order centred differences. The velocity field is solved by a parallel generalised minimal residual method (Saad, 2003) and the pressure field by a modified parallel three-dimensional Vcycle multigrid solver based on the work of Kwak and Lee (2004) and described in Shin et al. (2017). Parallelisation is achieved using an algebraic domain decomposition where communication across processes is handled by Message Passing Interface protocols.

The chosen PBT shown in figure 1(a) and described in the beginning of this section is built using a combination of primitive geometric objects (planes, cylinders and rectangular blocks) where each object is defined by a static distance function $\psi(x, y, z)$, positive in the fluid and negative in the solid. The resulting shape in figure 1(a) corresponds to the iso-value $\psi(x, y, z) = 0$. Details on how to construct similar complex objects are described in Kahouadji et al. (2018).

The temporal scheme is based on a second-order Gear method (Tucker, 2014) with implicit solution of the viscous terms of the velocity components. The time step Δt is chosen at each temporal iteration

in order to satisfy a criterion based on

$$\Delta t = \min\{\Delta t_{cap}, \Delta t_{vis}, \Delta t_{CFL}, \Delta t_{int}\} \quad (2.15)$$

where Δt_{cap} , Δt_{vis} , Δt_{CFL} and Δt_{int} represent the capillary, viscous, Courant–Friedrichs–Lewy (CFL) and interfacial CFL time steps, respectively, defined by

$$\Delta t_{cap} \equiv \frac{1}{2} \left(\frac{(\rho_o + \rho_w) \Delta x_{min}^3}{\pi \sigma} \right)^{1/2}, \quad \Delta t_{vis} \equiv \min \left(\frac{\rho_w}{\mu_w}, \frac{\rho_o}{\mu_o} \right) \frac{\Delta x_{min}^2}{6}, \quad (2.16a,b)$$

$$\Delta t_{CFL} \equiv \min_j \left(\min_{domain} \left(\frac{\Delta x_j}{u_j} \right) \right), \quad \Delta t_{int} \equiv \min_j \left(\min_{\Gamma(t)} \left(\frac{\Delta x_j}{\|V\|} \right) \right), \quad (2.17a,b)$$

where $\Delta x_{min} = \min_j(\Delta x_j)$ refers to the minimum size x at a given cell j , u_j , and V are the maximum fluid and interface velocities, respectively.

Mass is conserved to within ± 0.02 in all of our simulations. Our numerical procedure (Shin et al., 2018) has also been employed to simulate aeration in gas–liquid mixing (Kahouadji et al., 2022), vortex-interface dynamics and dispersion formation in turbulent water jets injected into an oil medium (Constante-Amores, 2021; Constante-Amores et al., 2021b, 2020b), the breakup of ligaments (Constante-Amores et al., 2020a), the coalescence of drops with interfaces (Constante-Amores et al., 2021a), the bursting of bubbles through interfaces (Constante-Amores et al., 2021c) and the dynamics of falling films (Batchvarov et al., 2020). We have also carried out a validation study against the experimental work of Hančil and Rod (1988); the results are in the Supplementary Information. To give an insight into the computational requirement, the current simulations are implemented based on the High Performance Computing service of Imperial College London, using 2 nodes of 48 CPUs for each case. All of the studied cases were computed in parallel, which took the authors two months to complete (corresponding to 25 revolutions of the impeller in this work).

3. Results and discussion

In this section, we present the spatio-temporal evolution of oil–water emulsion formation in the stirred vessel with a 4-pitch-blade turbine. First, a discussion of the vortical flow structures, and associated interfacial dynamics, is provided for the full range of Re and We studied starting with the flows generated for the lowest rotational speeds. Then, the results of an examination of the drop size distribution evolution and its dependence on Re and We are presented.

3.1. Flow structures

The evolution of the flows for the two phases in the (x, z) plane at $y = 4.25$ shows the existence of a rich dynamics, as demonstrated by the example depicted in figure 2 for the lowest Reynolds and Weber numbers studied, $Re = 1802$ and $We = 2.19$. A large primary vortex is created at early times ($t = 0.5 \times T$, see figure 2b), which starts at the blade tips toward the bottom of the vessel and then develops upwards near the vessel wall toward the interface. A small secondary vortex is also generated near the bottom of the impeller, which rotates radially in the opposite direction compared with the primary vortex. A suite of vortical structures accompany the development of the primary vortex which correspond to Moffatt, blade tip, Kelvin–Helmholtz and wall-end vortices (see figure 2c–e). As the velocity is continuous across the interface, and the flow in the oil phase is dragged radially inward with the meridional flow in the water phase, a large vortex is also generated in the oil phase which has the opposite circulation to that in the water. At $t = 6 \times T$, a swirling flow is observed near the interface in the water, which centrifuges the upper oil adjacent to it radially outward generating a small vortex of opposite circulation to the large one (see figure 2f). At $t = 9.5 \times T$, a small vortex breakdown appears at the interface in the oil (see figure 2g)

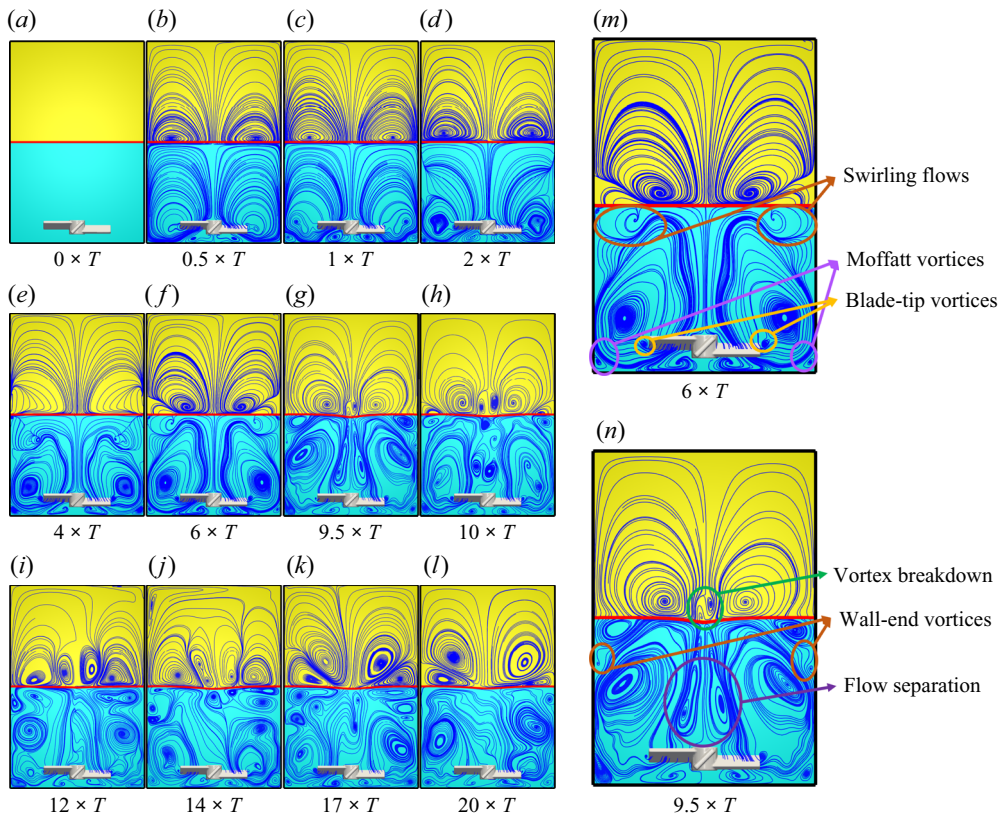


Figure 2. Spatio-temporal evolution of the vortical structures for $Re = 1802$ and $We = 2.19$ from an initial static state (a) until $t = 20 \times T$ (l). In this and subsequent figures, the results are displayed in the (x, z) plane at $y = 4.25$, and cyan and yellow are used to designate the water and oil phases, respectively, while the red solid line represents the interface location. Enlarged snapshots of the vortical structures with corresponding annotations are shown for $t = 6 \times T$ and $t = 9.5 \times T$ in (m) and (n), respectively.

which grows, squeezing the large meridional flow to the fixed sidewall until it gives way to two large circulation cells with a direction of radially outward (figure 2h–k); we will discuss vortex breakdown at higher Re and We below. The oil flow then remains in a configuration where the original meridional flow is confined to a thin layer in the vicinity of interface while the counter one above dominates in the oil phase (see figure 2l). On the other hand, flow separation (figure 2g) occurs in the water close to the edge of the rotating impeller (as described in the work of Piva & Meiburg, 2005). The water flow is characterised by a high level of turbulence involving the development of a multitude of vortices of varying scales. Similar behaviour in the water phase was demonstrated by Kahouadji et al. (2022) who carried out simulations of air–water mixing in stirred vessels.

We now present the spatio-temporal evolution of the interface shape for $Re = 7210$ and $We = 35$ in figure 3. As the impeller rotates, the azimuthal velocity generated by the impeller exerts a torque on the interface deforming it and subsequently drags the oil in the centre downwards (see figure 3a,b). The impeller rotation is not sufficiently rapid so as to cause the interface to reach the impeller; instead, the interface deforms into a helical shape, as shown in figure 3(c). Afterwards, a long ligament detaches from the deforming interface, which subsequently breaks into a large drop and several smaller ones (figure 3d,e). When $t > 14 \times T$, the dispersed large drop retracts to the deforming interface, spirally stretching in the meantime to become longer and thinner before attaching to the impeller (see figure 3f–i). The ligament detachment, breakup and retraction cycle is repeated

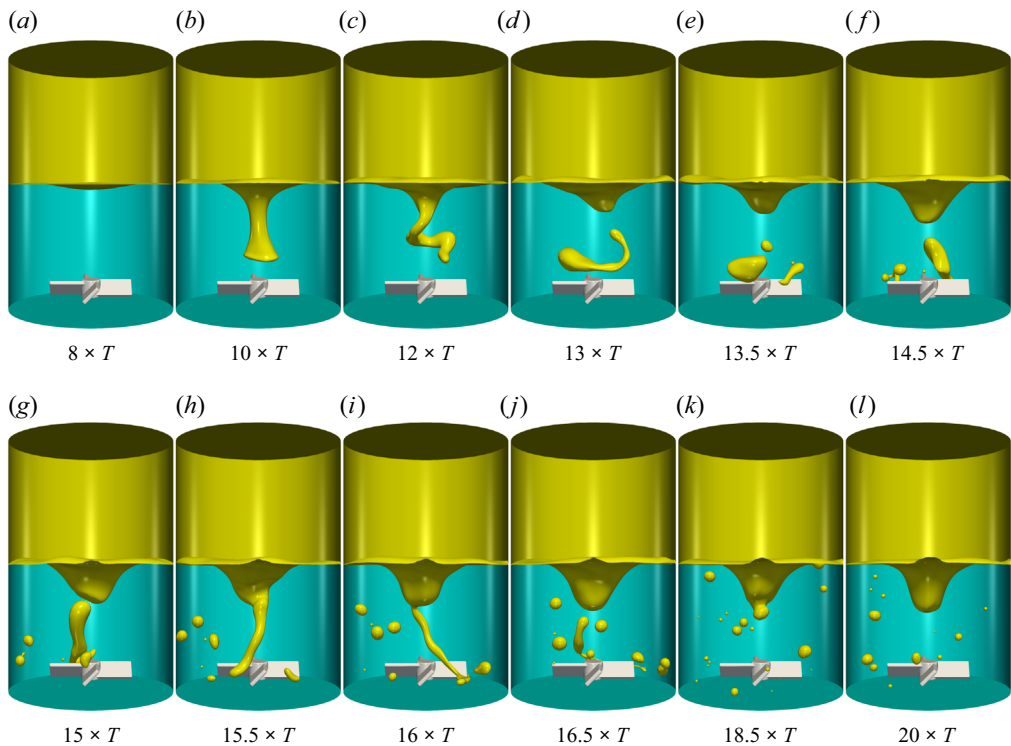


Figure 3. Spatio-temporal evolution of interface for $Re = 7210$ and $We = 35$ from a state where the interface starts to deform (a) until $t = 20 \times T$ (l).

until the system reaches a dynamic steady state where small drops remain dispersed in the water phase together with the deforming interface in the shape of a Newton's Bucket (see figure 3j–l). The existence of both ligament retraction, due to the action of interfacial tension, and elongation, due to the interaction with the turbulent flow in the water phase, highlights the presence of the delicate interplay amongst the various competing forces which results in the complexity associated with the mixing process.

An enlarged view of the breakup process is provided in figure 4, which presents the concurrence of multiple drop pinch-offs along one single ligament. Close inspection reveals that the ligament initially takes time to elongate and thin giving rise to thread-like regions between nodules, which continue to thin until they break up into individual droplets via a Rayleigh–Plateau mechanism. To explain the phenomenon observed within our mixing system, we examine closely the vorticity profiles around the ligament. Figure 5 presents four horizontal planes that depict the flow, coloured according to the magnitude of the vorticity. As shown in these plots, which also illustrate the position of the ligament relative to the vorticity distribution in the flow, the ligament lies in the high vorticity region generated by the impeller rotation. The interaction of the vorticity with the interface contributes to the instability of the ligament and this is particularly pronounced in the near-impeller regions in which the magnitude of the vorticity is significantly larger than those close to the vessel walls.

Next, we return to the occurrence of vortex breakdown in the oil phase which we had discussed above and note that it is also observed in the range of $Re = 1802$ – 9013 and $We = 2.19$ – 55 where the interface remains in a dynamic steady state assuming a Newton's Bucket-like shape, as shown in figure 6. The top panels of figure 6 highlight the vortical structures when the flow has reached a dynamic steady state where the vortex breakdown has developed into the dominant circulation cells along with the counter-rotating ones confined to a thin layer near the interface. For the higher Re and We cases

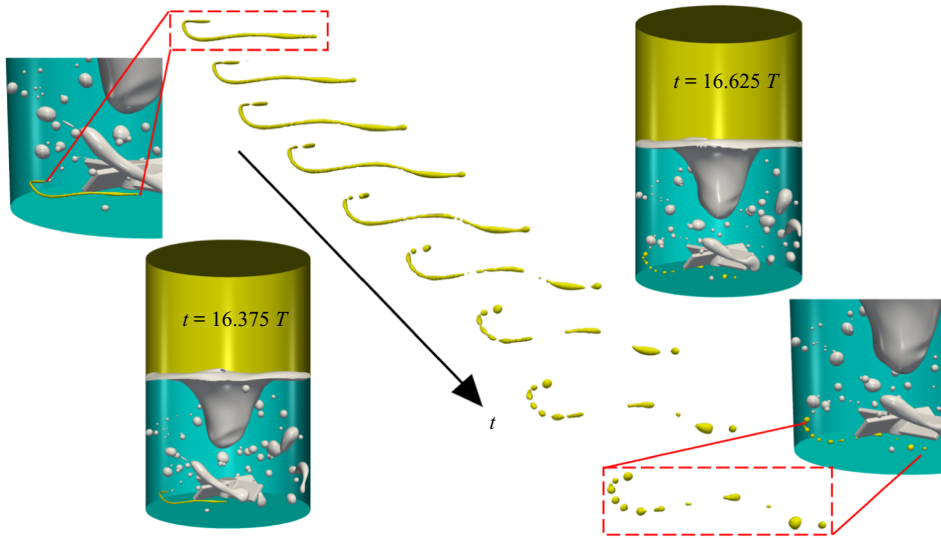


Figure 4. Enlarged views of ligament breakup for $Re = 9013$ and $We = 55$ at $16.375T$ and $16.625T$.

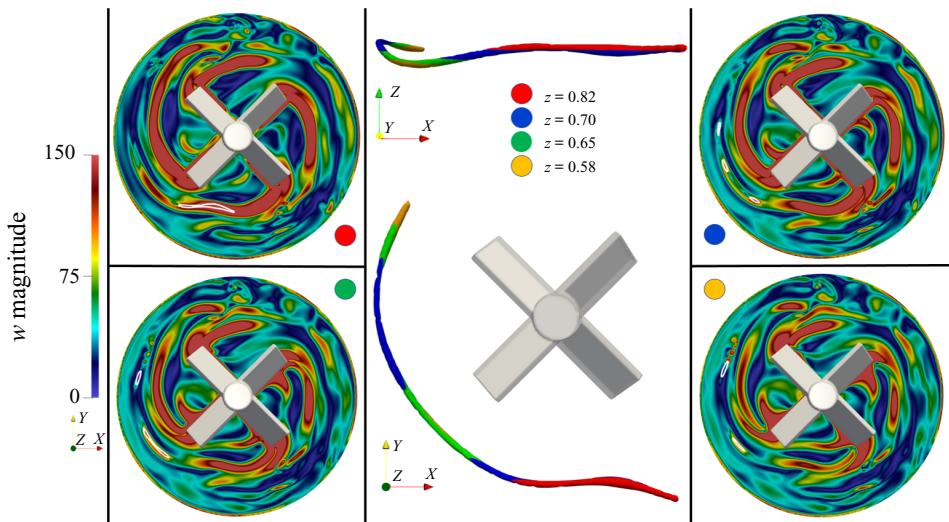


Figure 5. Vorticity in the ligament surroundings for $Re = 9013$ and $We = 55$. Four horizontal planes generated for $z = 0.82, 0.70, 0.65, 0.58$, corresponding to the red-, blue-, green- and yellow-labelled planes, are coloured according to the vorticity magnitude. The side and top views of the ligament shown in the middle and parts of the ligament are highlighted by white solid lines in the vorticity panels.

shown in figure 6(a–e), the vortex breakdown appears earlier, for example, at around $t = 7 \times T$ for $(Re, We) = (9013, 55)$ compared with $t = 9.5 \times T$ for $(Re, We) = (1802, 2.19)$ as shown in figure 2.

The bottom panels of figure 6 also show that, with increased Re and We , the depth of Newton’s Bucket increases, approaching the impeller with the interface assuming a teardrop shape. It may be possible to use the onset of vortex breakdown as an indicator of, and a surrogate for, the fact that the interface will remain sufficiently far from the impeller, and therefore unattached to it, at steady state. A methodology that focuses on the detection of vortex breakdown (if it occurs) for a given set of parameters, and then tracks the dependence of the breakdown over a range of such parameters, can lead to a map in (Re, We)

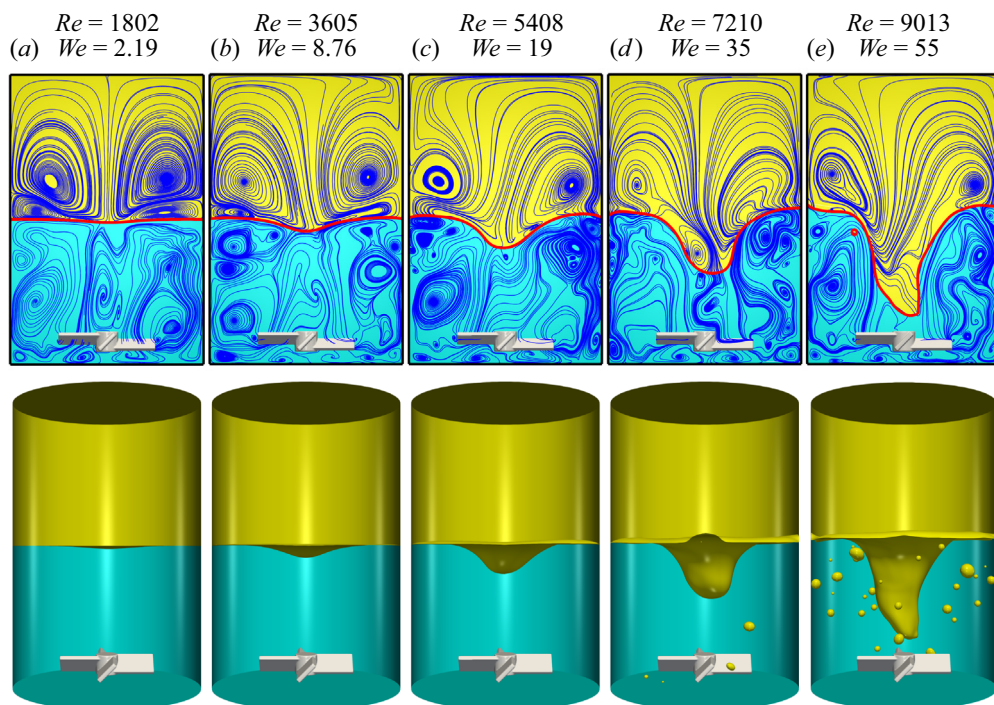


Figure 6. Vortical flow structures, top panels, and their corresponding interfacial shape, bottom panels, for (Re, We) combinations of $(1802, 2.19)$, $(3605, 8.76)$, $(5408, 19)$, $(7210, 35)$ and $(9013, 55)$ shown in (a–e), respectively, at $t = 25 \times T$ when the flow has reached a dynamic steady state.

space in which the region of limited mixing is demarcated; such an approach would obviate the need for lengthy computations to resolve the intricate and rapidly evolving interfacial dynamics.

We now consider a range of Re and We for which no retraction of the deforming interface from the impeller is observed. In figure 7, we show the spatio-temporal evolution of the vortical structures for $Re = 12\,618$ and $We = 107$ from an early-time state (at $t = 2 \times T$, see figure 7a) to a stage of the flow at which the deforming interface has reached the impeller (at $t = 9 \times T$, see figure 7f). During the early stages of the flow, the vortical structures observed are similar to those depicted in figure 2 discussed above. Instead of the appearance of vortex breakdown seen at lower Re and We , the streamline configuration at higher Re and We indicates a strong tendency of the interface to be deflected towards the impeller (see figure 7e). Although the water phase is dominated by the primary vortex, there are a number of secondary vortices close to the vessel sidewall in the vicinity of the interface which act to pump the water upward along the wall (see figure 7c–f). In figure 8, we illustrate the spatio-temporal evolution of interface shape for $(Re, We) = (10\,816, 78)$ and $(12\,618, 107)$ shown for $t = 8–25 \times T$. After the interface reaches the impeller (see figure 8b), it is further stretched radially and long oil ligaments are created when the impeller blades cut through the rotating curtains (see figure 8c). Long ligaments subsequently stretch to become thinner until pinch-off occurs, giving rise to multitudes of smaller drops (see figure 8d). Then, the deforming interface evolves differently depending on the value of Re and We . Whereas for $Re = 9013$ and $We = 55$ the interface eventually detaches from the impeller and no further ligaments are generated, as shown in figure 4, the formation of new ligaments remains in place at the higher Re and We (see figure 8e). The small drops created from ligament breakup either travel upwards under the action of buoyancy, eventually merging with the oil phase, or remain dispersed in water until they coalesce with other drops. As a result, although the number of dispersed drops decreases with time for $Re = 9013$ and $We = 55$, this is not the case at higher Re and We as the drops ‘lost’ due to coalescence

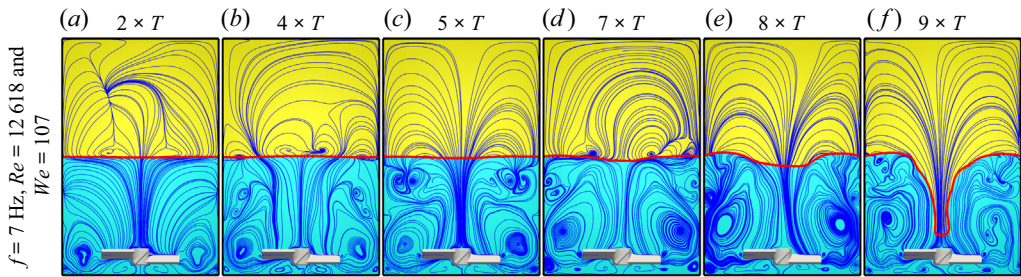


Figure 7. Spatio-temporal evolution of the vortical structures for $Re = 12\,618$ and $We = 107$ at $t = 2 - 9 \times T$ shown in (a–f), respectively.

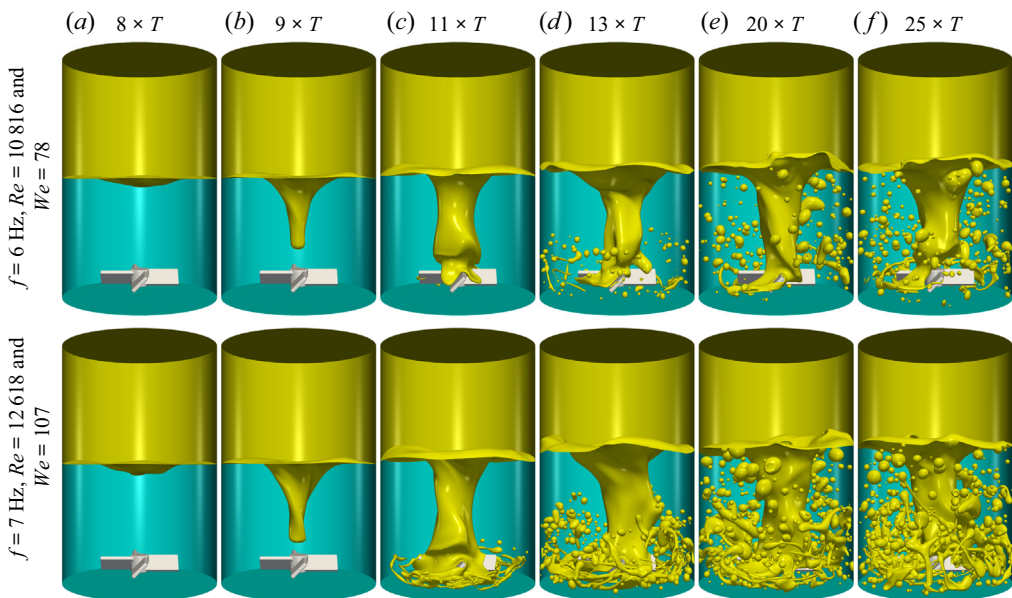


Figure 8. Spatio-temporal evolution of the interface toward the development of an oil-in-water emulsion for $(Re, We) = (10\,816, 78)$ and $(12\,618, 107)$ shown in the top and bottom panels, respectively, for $t = 8 \times T$ between $25 \times T$ in (a–f), respectively.

with the oil–water interface are replenished via continual ligament formation and subsequent breakup (see figure 8f). A discussion of the evolution of the dispersed drop number and size distribution will be provided in § 3.2.

At larger Re and We , the vortical structures in the oil and water phases during the early and intermediate stages of the dynamics resemble those discussed above; this is exemplified by figures 9(a)–9(f) in which we show the evolution of these structures for $Re = 18\,026$ and $We = 219$ between $t = 2 \times T$ and $9 \times T$ which culminates in the interface reaching the impeller. Inspection of figure 9(g–l), however, in which we illustrate the evolving interfacial dynamics, reveals that drop coalescence dominates over breakup. In contrast to the lower Re and We cases discussed above, a larger torque is generated in the present case which results in a deforming interface of a helical shape with four rotating curtains (see figure 9g). Following their formation, the long ligaments merge to form a relatively large mass of oil that collects around the bottom of the vessel before breaking up into smaller drops as they are rapidly and continually created from the impeller tips (see figure 9h). As can be seen in figure 9(i), the dispersed phase in this high Re case is composed mainly of stretched oil ligaments rather than the individual drops observed to

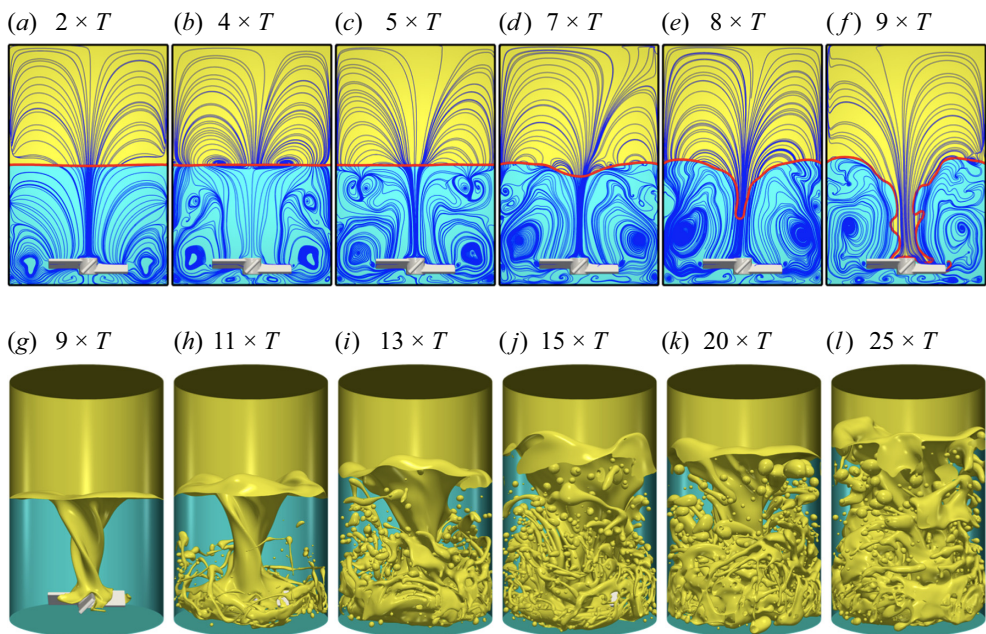


Figure 9. Spatio-temporal evolution of the vortical structure between $t = 2 \times T$ and $9 \times T$, (a–f), and of the interface between $t = 9 \times T$ and $25 \times T$, (g–l), for $Re = 18\,026$ and $We = 219$.

accompany the flow at lower Re . With increasing time, an increasing amount of oil is entrained into the water phase; as a result, the latter is displaced upwards along the vessel sidewalls lifting the interface as can be seen in figure 9(j,k). At $t = 25 \times T$, the dynamics is characterised by complex interfacial topology. It is notable that the number of small droplets has decreased due to coalescence giving way to large dispersed-phase structures resulting from the merging of ligaments and drops, as shown in figure 9(l). The drop size distribution as a function of the impeller speed is discussed next.

3.2. Drop size distribution

From an industrial point of view, it is often important to track the evolution of the dispersed-phase statistics and metrics in terms of number of drops, their size distribution, the interfacial area and hold up. Figure 10 presents the temporal evolution of the number of dispersed drops ($t = 5\text{--}25 \times T$) for $f = 5\text{--}10$ Hz ($Re = 9013\text{--}18\,026$ and $We = 55\text{--}219$), along with the corresponding interface shapes at $t = 25 \times T$. For all displayed frequencies, no dispersed drop appears until there is a steep increase from zero drop count at $t \approx 8 \times T$, caused by the above-mentioned Rayleigh–Plateau-type breakup from long ligaments. In addition, the appearance of the dispersed drops occurs earlier with increasing impeller speed due to the accelerated deviation of the interface and its earlier interaction with the impeller to produce ligaments. Furthermore, figures 8(c) and 9(h) provide clear evidence that, when the rotation frequency is increased, a larger part of the deforming interface contacts the impeller and therefore more ligaments are produced at the beginning, which corresponds to the steeper increase, as shown in figure 10. After that, the number of dispersed oil drops for $f = 5$ Hz falls off gently since the deforming interface no longer makes contact with the impeller while dispersed drops tend to coalesce with the oil overlying the water phase. With increasing frequency, the dispersed oil drop number continues to increase until the breakup rate balances that of coalescence. For cases with $f \geq 8$ Hz, an over-shooting peak is observed before the number decreases towards a dynamic steady state. We posit that this phenomenon is due to the fact that the larger amount of ligaments and drops produced simultaneously increases the coalescence

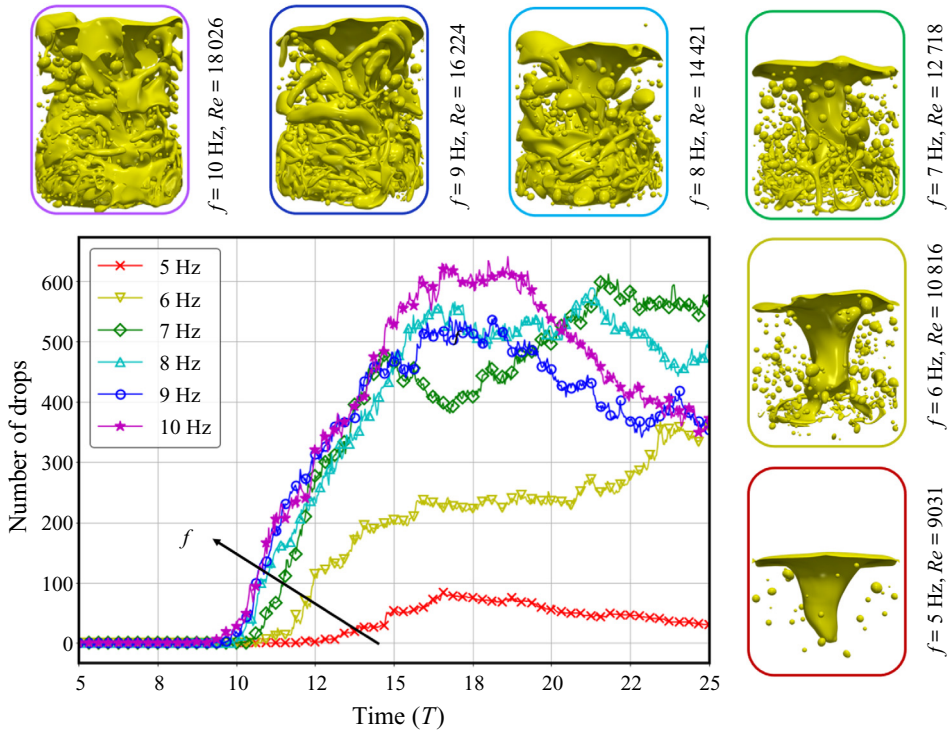


Figure 10. Temporal evolution of the number of dispersed drops for frequencies $f = 5, 6, 7, 8, 9, 10$ Hz, which correspond to $Re = 9013\text{--}18026$ and $We = 55\text{--}219$. Snapshots of the interface shapes at $t = 25 \times T$ are also presented for each frequency. The black arrow indicates the earlier drop occurrence and the steeper increase from zero drop count when impeller speed is increased.

probability in the system. As a result, there exists a stage where the coalescence rate is larger than the breakup rate, giving rise to the reduction in drop counts.

It is evident from figure 10 that the steady number of dispersed drops has a non-monotonic dependence on the impeller speed while its over-shooting peak increases with increasing rotation frequencies. On the other hand, our results also indicate that the interfacial area of the dispersed phase at steady state ($t = 25 \times T$) shows no such dependence as shown in figure 11(a). This interfacial area is calculated as A_d/A_{cap} , where A_d refers to the surface area of all dispersed drops and A_{cap} is the sphere surface area with the capillary length as its diameter. The interfacial area appears to be proportional to the increased impeller speed (up to $f = 10$ Hz) even though the number of dispersed drops reaches its peak at an intermediate frequency ($f = 7$ Hz). The reason for this is that at larger frequencies, long ligaments, with larger interfacial area, dominate the dispersed-phase morphology (see figure 9). From figure 11(a), the optimal impeller speed can be selected depending on the relative importance of the interfacial area and dispersed drop number to the particular application in question.

For all frequencies, we examine the drop size distribution at $t = 25 \times T$ for $f = 5\text{--}10$ Hz ($Re = 9013\text{--}18\,026$ and $We = 55\text{--}219$). We define a dimensionless ‘drop’ size as V_d/V_{cap} , where V_d refers to the volume of a dispersed phase entity (which can be a deformed drop or a ligament) and V_{cap} is a spherical drop whose diameter corresponds to the capillary length scale, $\sqrt{\sigma/\Delta\rho}$; here, $\Delta\rho$ is the difference in density between the oil and water phases. A box plot distribution of V_d/V_{cap} at $t = 25 \times T$ is shown in figure 11(b) indicating that the overall trend is that an increase in frequency leads to a narrower distribution and smaller median drop size, which is consistent with the conclusion of previous studies (Pacek et al., 1998; Zhou & Kresta, 1998b). This trend is also demonstrated in figure 12 where the fitted drop size distribution is plotted against logarithmic V_d/V_{cap} . For $f = 5$ Hz, the drop size is best fitted

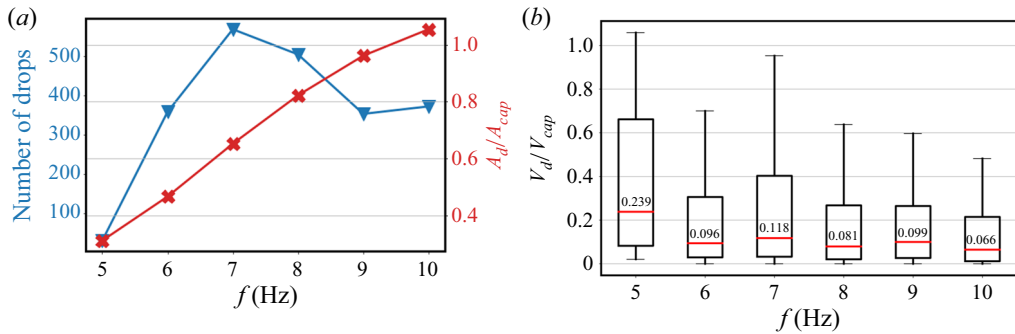


Figure 11. (a) Number of drops (blue line, inverted triangle markers) and interfacial area (red line, cross-shaped markers) of the dispersed oil phase. (b) Box plot distribution of the drop size (outliers are not shown here), at $t = 25 \times T$ for frequencies $f = 5, 6, 7, 8, 9, 10$ Hz, which correspond to $Re = 9013\text{--}18\,026$ and $We = 55\text{--}219$. Here, the median value of V_d/V_{cap} is indicated by the horizontal red lines.

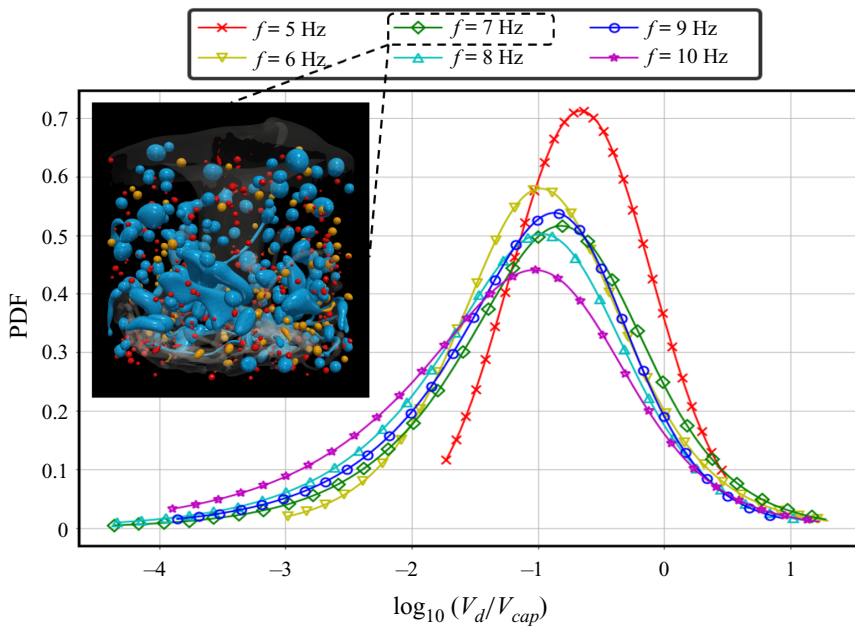


Figure 12. Drop size distribution of the dispersed oil phase at $t = 25 \times T$ for $f = 5, 6, 7, 8, 9, 10$ Hz ($Re = 9013\text{--}18\,026$ and $We = 55\text{--}219$). The attached image shows a drop size map for $f = 7$ Hz at $t = 25 \times T$ where all the dispersed phases are coloured by red, yellow and blue according to their size as small, moderate and large, respectively.

to a normal distribution, while for higher impeller speeds, the drop size follows a generalised logistic distribution. The narrow distribution for $f = 5$ Hz indicates that relatively large (median value to the left figure 12) drops of well-distributed size are produced; on the other hand, with increasing impeller speed, the median drop size moves to smaller sizes, while a skewed shape towards the more frequently produced small drops is observed. Additionally, a drop size map for $f = 7$ Hz is also shown in figure 12 where all the dispersed-phase entities are classified into three size categories and coloured accordingly. This gives a clear indication that the ‘large-sized’ drops contain the long ligaments that have not broken

up entirely, whereas the ‘small-’ and ‘moderate-sized’ drops are composed of individual droplets of various sizes.

4. Conclusion and perspective

In this paper, using our high-fidelity three-dimensional simulations, we study the effect of impeller rotational speed on the complex interfacial dynamics during oil–water mixing in a stirred vessel with a 4-pitch-blade turbine; we explore rotational speeds in the range $f = 1\text{--}10$ Hz, which correspond to Reynolds and Weber number ranges of $Re = 1802\text{--}18\,026$ and $We = 2.19\text{--}219$, respectively. We have shown that the interface shape and vortical structures within such a system are strongly dependent on the impeller speed. In particular, we have demonstrated the possibility of using vortex breakdown as an indicator that the interface undergoes little breakup due to very little interaction with the impeller. In addition, we have also presented a drop size analysis over the full range of frequencies studied in terms of temporal evolution of the dispersed drop number and its size distribution at steady state, and shown that an optimal impeller speed can be selected depending on the needs of the application in question. In future research, it can be interesting to explore other effects on the mixing system, which include impeller geometry, fluid phase rheology and the presence of surfactants; the latter are of particular interest since surfactants may be present in the system either as a contaminant or by design.

Funding. This work is supported by the Engineering & Physical Sciences Research Council, UK, through the MEMPHIS (EP/K003976/1) and PREMIERE (EP/T000414/1) Programme Grants, and by computing time at HPC facilities provided by the Research Computing Service of Imperial College London. D.J. and J.C. acknowledge support through HPC/AI computing time at the Institut du Développement et des Ressources en Informatique Scientifique (IDRIS) of the Centre National de la Recherche Scientifique (CNRS), coordinated by GENCI (Grand Equipement National de Calcul Intensif) Grant 2022 A0122B06721. O.K.M. also acknowledges funding from PETRONAS and the Royal Academy of Engineering for a Research Chair in Multiphase Fluid Dynamics, and the PETRONAS Centre for Engineering of Multiphase Systems. Simulations have been performed using code BLUE (Shin et al., 2017) and the visualisations have been generated using Paraview.

Declaration of interest. The authors report no conflict of interest.

Author contributions. O.K.M. secured the funding; F.L., L.K., J.P.V., D.J. and O.K.M. contributed to the design of the research plan and manuscript editing; F.L., L.K., S.S., J.C. and D.J. contributed to the computations.

Data availability statement. Raw data are available from the corresponding author L.K.

Ethical standards. The research meets all ethical guidelines, including adherence to the legal requirements of the study country.

References

- Afshar Ghotli, R., Raman, A.A.A., Ibrahim, S., & Baroutian, S. (2013). Liquid-liquid mixing in stirred vessels: A review. *Chemical Engineering Communications*, 200(5), 595–627.
- Albernaz, D.L., Do-Quang, M., Hermanson, J.C., & Amberg, G. (2017). Droplet deformation and heat transfer in isotropic turbulence. *Journal of Fluid Mechanics*, 820, 61–85.
- Anderson, D.M., McFadden, G.B., & Wheeler, A.A. (1998). Diffuse-interface methods in fluid mechanics. *Annual Review of Fluid Mechanics*, 30(1), 139–165.
- Andersson, R., & Andersson, B. (2006). On the breakup of fluid particles in turbulent flows. *AIChE Journal*, 52(6), 2020–2030.
- Bakker, A., LaRoche, R.D., Wang, M.-H., & Calabrese, R.V. (1997). Sliding mesh simulation of laminar flow in stirred reactors. *Chemical Engineering Research and Design*, 75(1), 42–44.
- Batchvarov, A., Kahouadji, L., Magnini, M., Constante-Amores, C.R., Craster, R.V., Shin, S., Chergui, J., Juric, D., & Matar, O.K. (2020). Effect of surfactant on elongated bubbles in capillary tubes at high Reynolds number. *Physical Review Fluids*, 5, 093605.
- Becker, P.J., Puel, F., Chevalier, Y., & Sheibat-Othman, N. (2014). Monitoring silicone oil droplets during emulsification in stirred vessel: Effect of dispersed phase concentration and viscosity. *The Canadian Journal of Chemical Engineering*, 92(2), 296–306.
- Boxall, J.A., Koh, C.A., Sloan, E.D., Sum, A.K., & Wu, D.T. (2010). Measurement and calibration of droplet size distributions in water-in-oil emulsions by particle video microscope and a focused beam reflectance method. *Industrial & Engineering Chemistry Research*, 49(3), 1412–1418.
- Calabrese, R.V., Chang, T.P.K., & Dang, P.T. (1986). Drop breakup in turbulent stirred-tank contactors. Part I: Effect of dispersed-phase viscosity. *AIChE Journal*, 32(4), 657–666.

- Chiappini, D., Sbragaglia, M., Xue, X., & Falcucci, G. (2019). Hydrodynamic behavior of the pseudopotential lattice Boltzmann method for interfacial flows. *Physical Review E*, *99*, 053305.
- Chiu, P.-H., & Lin, Y.-T. (2011). A conservative phase field method for solving incompressible two-phase flows. *Journal of Computational Physics*, *230*(1), 185–204.
- Constante-Amores, C.R. (2021). *Three-dimensional computational fluid dynamics simulations of complex multiphase flows with surfactants* (PhD Thesis). Imperial College London, UK.
- Constante-Amores, C.R., Kahouadji, L., Batchvarov, A., Seungwon, S., Chergui, J., Juric, D., & Matar, O.K. (2020a). Dynamics of retracting surfactant-laden ligaments at intermediate Ohnesorge number. *Physical Review Fluids*, *5*, 084007.
- Constante-Amores, C.R., Kahouadji, L., Batchvarov, A., Seungwon, S., Chergui, J., Juric, D., & Matar, O.K. (2021a). Role of surfactant-induced marangoni stresses in drop-interface coalescence. *Journal of Fluid Mechanics*, *925*, A15.
- Constante-Amores, C.R., Kahouadji, L., Batchvarov, A., Shin, S., Chergui, J., Juric, D., & Matar, O.K. (2021b). Direct numerical simulations of transient turbulent jets: Vortex-interface interactions. *Journal of Fluid Mechanics*, *922*, A6.
- Constante-Amores, C.R., Kahouadji, L., Batchvarov, A., Shin, S., Chergui, J., Juric, D., & Matar, O.K. (2020b). Rico and the jets: Direct numerical simulations of turbulent liquid jets. *Physical Review Fluids*, *5*, 110501.
- Constante-Amores, C.R., Kahouadji, L., Batchvarov, A., Shin, S., Chergui, J., Juric, D., & Matar, O.K. (2021c). Dynamics of a surfactant-laden bubble bursting through an interface. *Journal of Fluid Mechanics*, *911*, A57.
- De Hert, S.C., & Rodgers, T.L. (2017). On the effect of dispersed phase viscosity and mean residence time on the droplet size distribution for high-shear mixers. *Chemical Engineering Science*, *172*, 423–433.
- Deardorff, J.W. (1970). A numerical study of three-dimensional turbulent channel flow at large Reynolds numbers. *Journal of Fluid Mechanics*, *41*(2), 453–480.
- Derksen, J.J. (2003). Numerical simulation of solids suspension in a stirred tank. *AIChE Journal*, *49*(11), 2700–2714.
- Derksen, J.J. (2011). Blending of miscible liquids with different densities starting from a stratified state. *Computers & Fluids*, *50*(1), 35–45.
- Derksen, J.J. (2012). Direct simulations of mixing of liquids with density and viscosity differences. *Industrial & Engineering Chemistry Research*, *51*(19), 6948–6957.
- Derksen, J., & Van den Akker, H.E.A. (1999). Large eddy simulations on the flow driven by a Rushton turbine. *AIChE Journal*, *45*(2), 209–221.
- Di Ilio, G., Krastev, V.K., & Falcucci, G. (2019). Evaluation of a scale-resolving methodology for the multidimensional simulation of GDI sprays. *Energies*, *12*, 2699.
- Eggels, J.G.M. (1996). Direct and large-eddy simulation of turbulent fluid flow using the lattice-Boltzmann scheme. *International Journal of Heat and Fluid Flow*, *17*(3), 307–323.
- El-Hamouz, A., Cooke, M., Kowalski, A., & Sharratt, P. (2009). Dispersion of silicone oil in water surfactant solution: Effect of impeller speed, oil viscosity and addition point on drop size distribution. *Chemical Engineering and Processing*, *48*(2), 633–642.
- Fadlun, E., Verzicco, R., Orlandi, P., & Mohd-Yusof, J. (2000). Combined immersed-boundary finite-difference methods for three-dimensional complex flow simulations. *Journal of Computational Physics*, *161*, 35–60.
- Falcucci, G., & Ubertini, S. (2010). Lattice Boltzmann modeling of diesel spray formation and break-up. *SAE International Journal of Fuels and Lubricants*, *3*, 582–593.
- Giapos, A., Pachatouridis, C., & Stamatoudis, M. (2005). Effect of the number of impeller blades on the drop sizes in agitated dispersions. *Chemical Engineering Research and Design*, *83*(12), 1425–1430.
- Gillissen, J.J.J., & Van den Akker, H.E.A. (2012). Direct numerical simulation of the turbulent flow in a baffled tank driven by a Rushton turbine. *AIChE Journal*, *58*(12), 3878–3890.
- Hančil, V., & Rod, V. (1988). Break-up of a drop in a stirred tank. *Chemical Engineering and Processing: Process Intensification*, *23*(3), 189–193.
- Harlow, F.H., & Welch, J.E. (1965). Numerical calculation of time-dependent viscous incompressible flow of fluid with free surface. *The Physics of Fluids*, *8*(12), 2182–2189.
- Harvey, P.S., & Greaves, M. (1982). Turbulent flow in an agitated vessel, II: Numerical solution and model predictions. *Transactions of the Institution of Chemical Engineers*, *60*, 201.
- Hasan, B.O. (2017). Breakage of drops and bubbles in a stirred tank: A review of experimental studies. *Chinese Journal of Chemical Engineering*, *25*(6), 698–711.
- Hinze, J.O. (1955). Fundamentals of the hydrodynamic mechanism of splitting in dispersion processes. *AIChE Journal*, *1*(3), 289–295.
- Hirt, C.W., & Nichols, B.D. (1981). Volume of fluid (VOF) method for the dynamics of free boundaries. *Journal of Computational Physics*, *39*(1), 201–225.
- Ibarra, R. (2017). *Horizontal and low-inclination oil-water flow investigation using laser-based diagnostic techniques* (PhD Thesis). Imperial College London, UK.
- Kahouadji, L., Liang, F., Valdes, J., Chergui, J., Juric, D., Shin, S., Craster, R.V., & Matar, O.K. (2022). The transition to aeration in turbulent two-phase mixing in stirred vessels. *Flow* (submitted).
- Kahouadji, L., Nowak, E., Kovalchuk, N., Chergui, J., Juric, D., Shin, S., Simmons, M.J.H., Craster, R.V., & Matar, O.K. (2018). Simulation of immiscible liquid–liquid flows in complex microchannel geometries using a front-tracking scheme. *Microfluidics and Nanofluidics*, *22*(11), 1–12.

- Komrakova, A.E. (2019). Single drop breakup in turbulent flow. *The Canadian Journal of Chemical Engineering*, 97(10), 2727–2739.
- Konno, M., Aoki, M., & Saito, S. (1983). Scale effect on breakup process in liquid-liquid agitated tanks. *Journal of Chemical Engineering of Japan*, 16(4), 312–319.
- Kraume, M., Gäbler, A., & Schulze, K. (2004). Influence of physical properties on drop size distribution of stirred liquid-liquid dispersions. *Chemical Engineering & Technology: Industrial Chemistry-Plant Equipment-Process Engineering-Biotechnology*, 27(3), 330–334.
- Kwak, D.Y., & Lee, J.S. (2004). Multigrid algorithm for the cell-centered finite difference method II: Discontinuous coefficient case. *Numerical Methods for Partial Differential Equations: An International Journal*, 20(5), 742–764.
- Lilly, D.K. (1966). *On the application of the eddy viscosity concept in the inertial sub-range of turbulence* (NCAR Manuscript 123). Boulder, CO.
- Lilly, D.K. (1967). The representation of small-scale turbulence in numerical simulation experiments. *Proc. IBM Sci. Comput. Symp. Environ. Sci.* (1967), 195–210.
- Lovick, J., Mouza, A.A., Paras, S.V., Lye, G.J., & Angeli, P. (2005). Drop size distribution in highly concentrated liquid-liquid dispersions using a light back scattering method. *Journal of Chemical Technology & Biotechnology: International Research in Process, Environmental & Clean Technology*, 80(5), 545–552.
- Luo, J.Y., & Gosman, A.D. (1994). *Prediction of impeller-induced flow in mixing vessels using multiple frames of reference*. Institute of Chemical Engineers Symposium Series, 136, 549–556.
- Maaß, S., Gäbler, A., Zaccone, A., Paschedag, A.R., & Kraume, M. (2007). Experimental investigations and modelling of breakage phenomena in stirred liquid/liquid systems. *Chemical Engineering Research and Design*, 85(5), 703–709.
- Maaß, S., & Kraume, M. (2012). Determination of breakage rates using single drop experiments. *Chemical Engineering Science*, 70, 146–164.
- Maaß, S., Metz, F., Rehm, T., & Kraume, M. (2010). Prediction of drop sizes for liquid-liquid systems in stirred slim reactors—part I: Single stage impellers. *Chemical Engineering Journal*, 162(2), 792–801.
- Maaß, S., Wollny, S., Sperling, R., & Kraume, M. (2009). Numerical and experimental analysis of particle strain and breakage in turbulent dispersions. *Chemical Engineering Research and Design*, 87(4), 565–572.
- McMillan, O.J., & Ferziger, J.H. (1979). Direct testing of subgrid-scale models. *AIAA Journal*, 17(12), 1340–1346.
- Meyers, J., & Sagaut, P. (2006). On the model coefficients for the standard and the variational multi-scale Smagorinsky model. *Journal of Fluid Mechanics*, 569, 287–319.
- Mohd-Yusof, J. (1997). *Combined immersed boundaries/B-splines methods for simulations of flows in complex geometries (CTR Annual Research Briefs)*. NASA Ames/Stanford University.
- Nachtigall, S., Zedel, D., & Kraume, M. (2016). Analysis of drop deformation dynamics in turbulent flow. *Chinese Journal of Chemical Engineering*, 24(2), 264–277.
- Nachtigall, S., Zedel, D., Maass, S., Walle, A., Schäfer, M., & Kraume, M. (2012). Determination of drop breakage mechanisms by experimental and numerical investigations of single drop breakages. In *14th European Conference on Mixing, 10–13 September, Warsaw, Poland*.
- Naeeni, S.K., & Pakzad, L. (2019a). Droplet size distribution and mixing hydrodynamics in a liquid-liquid stirred tank by CFD modeling. *International Journal of Multiphase Flow*, 120, 103100.
- Naeeni, S.K., & Pakzad, L. (2019b). Experimental and numerical investigation on mixing of dilute oil in water dispersions in a stirred tank. *Chemical Engineering Research and Design*, 147, 493–509.
- Pacek, A.W., Man, C.C., & Nienow, A.W. (1998). On the sauter mean diameter and size distributions in turbulent liquid/liquid dispersions in a stirred vessel. *Chemical Engineering Science*, 53(11), 2005–2011.
- Peskin, C.S. (1977). Numerical analysis of blood flow in the heart. *Journal of Computational Physics*, 25(3), 220–252.
- Piva, M., & Meiburg, E. (2005). Steady axisymmetric flow in an open cylindrical container with a partially rotating bottom wall. *Physics of Fluids*, 17(6), 063603.
- Pope, S.B. (2000). *Turbulent flows*. Cambridge University Press.
- Pope, S.B. (2004). Ten questions concerning the large-eddy simulation of turbulent flows. *New Journal of Physics*, 6(1), 35.
- Qin, C., Chen, C., Xiao, Q., Yang, N., Yuan, C., Kunkelmann, C., Cetinkaya, M., & Mülheims, K. (2016). CFD-PBM simulation of droplets size distribution in rotor-stator mixing devices. *Chemical Engineering Science*, 155, 16–26.
- Ramkrishna, D. (2000). *Population balances: Theory and applications to particulate systems in engineering*. Elsevier.
- Roccon, A., De Paoli, M., Zonta, F., & Soldati, A. (2017). Viscosity-modulated breakup and coalescence of large drops in bounded turbulence. *Physical Review Fluids*, 2(8), 083603.
- Roudsari, S.F., Turcotte, G., Dhib, R., & Ein-Mozaffari, F. (2012). CFD modeling of the mixing of water in oil emulsions. *Computers & Chemical Engineering*, 45, 124–136.
- Saad, Y. (2003). *Iterative methods for sparse linear systems*. SIAM.
- Sanjuan-Galindo, R., Soto, E., Zenit, R., & Ascanio, G. (2015). Viscous filament fragmentation in a turbulent flow inside a stirred tank. *Chemical Engineering Communications*, 202(9), 1251–1260.
- Sathyagal, A.N., Ramkrishna, D., & Narsimhan, G. (1996). Droplet breakage in stirred dispersions. Breakage functions from experimental drop-size distributions. *Chemical Engineering Science*, 51(9), 1377–1391.
- Scapin, N., Dalla Barba, F., Lupo, G., Rosti, M.E., Duwig, C., & Brandt, L. (2022). Finite-size evaporating droplets in weakly compressible homogeneous shear turbulence. *Journal of Fluid Mechanics*, 934, A15.

- Scarbolo, L., Bianco, F., & Soldati, A. (2015). Coalescence and breakup of large droplets in turbulent channel flow. *Physics of Fluids*, 27(7), 073302.
- Scarbolo, L., Bianco, F., & Soldati, A. (2016). Turbulence modification by dispersion of large deformable droplets. *European Journal of Mechanics-B/Fluids*, 55, 294–299.
- Scarbolo, L., & Soldati, A. (2013). Turbulence modulation across the interface of a large deformable drop. *Journal of Turbulence*, 14(11), 27–43.
- Sethian, J.A., & Smereka, P. (2003). Level set methods for fluid interfaces. *Annual Review of Fluid Mechanics*, 35(1), 341–372.
- Shin, S. (2007). Computation of the curvature field in numerical simulation of multiphase flow. *Journal of Computational Physics*, 222(2), 872–878.
- Shin, S., Chergui, J., & Juric, D. (2017). A solver for massively parallel direct numerical simulation of three-dimensional multiphase flows. *Journal of Mechanical Science and Technology*, 31(4), 1739–1751.
- Shin, S., Chergui, J., Juric, D., Kahouadji, L., Matar, O.K., & Craster, R.V. (2018). A hybrid interface tracking–level set technique for multiphase flow with soluble surfactant. *Journal of Computational Physics*, 359, 409–435.
- Shin, S., & Juric, D. (2009a). A hybrid interface method for three-dimensional multiphase flows based on front tracking and level set techniques. *International Journal for Numerical Methods in Fluids*, 60(7), 753–778.
- Shin, S., & Juric, D. (2009b). Simulation of droplet impact on a solid surface using the level contour reconstruction method. *Journal of Mechanical Science and Technology*, 23(9), 2434–2443.
- Shu, S., & Yang, N. (2018). GPU-accelerated large eddy simulation of stirred tanks. *Chemical Engineering Science*, 181, 132–145.
- Smagorinsky, J. (1963). General circulation experiments with the primitive equations: I. The basic experiment. *Monthly Weather Review*, 91(3), 99–164.
- Sprow, F.B. (1967). Distribution of drop sizes produced in turbulent liquid–liquid dispersion. *Chemical Engineering Science*, 22(3), 435–442.
- Stamatoudis, M., & Tavlarides, L.L. (1985). Effect of continuous-phase viscosity on the drop sizes of liquid–liquid dispersions in agitated vessels. *Industrial & Engineering Chemistry Process Design and Development*, 24(4), 1175–1181.
- Tryggvason, G., Bunner, B., Esmaeeli, A., Juric, D., Al-Rawahi, N., Tauber, W., Han, J., Nas, S., & Jan, Y.-J. (2001). A front-tracking method for the computations of multiphase flow. *Journal of Computational Physics*, 169(2), 708–759.
- Tucker, P.G. (2014). *Unsteady computational fluid dynamics in aeronautics*. Dordrecht, the Netherlands: Springer.
- Tyagi, M., Roy, S., Harvey, A.D., III, & Acharya, S. (2007). Simulation of laminar and turbulent impeller stirred tanks using immersed boundary method and large eddy simulation technique in multi-block curvilinear geometries. *Chemical Engineering Science*, 62(5), 1351–1363.
- Unverdi, S.O., & Tryggvason, G. (1992). A front-tracking method for viscous, incompressible, multi-fluid flows. *Journal of Computational Physics*, 100(1), 25–37.
- Wang, C.Y., & Calabrese, R.V. (1986). Drop breakup in turbulent stirred-tank contactors. Part II: Relative influence of viscosity and interfacial tension. *AIChE Journal*, 32(4), 667–676.
- Zhou, G., & Kresta, S.M. (1998a). Correlation of mean drop size and minimum drop size with the turbulence energy dissipation and the flow in an agitated tank. *Chemical Engineering Science*, 53(11), 2063–2079.
- Zhou, G., & Kresta, S.M. (1998b). Evolution of drop size distribution in liquid–liquid dispersions for various impellers. *Chemical Engineering Science*, 53(11), 2099–2113.